Pramana – J. Phys. (2017) 88: 59
DOI 10.1007/s12043-017-1364-5

Dependence of *in-situ* Bose condensate size on final frequency of RF-field in evaporative cooling

S R MISHRA[1,2,*], S P RAM[1], S K TIWARI[1] and H S RAWAT[1,2]

[1]Raja Ramanna Centre for Advanced Technology, Indore 452 013, India
[2]Homi Bhabha National Institute, Mumbai 400 094, India
*Corresponding author. E-mail: srm@rrcat.gov.in

MS received 30 June 2016; revised 26 September 2016; accepted 5 October 2016; published online 8 March 2017

Abstract. We report the results of *in-situ* characterization of ^{87}Rb atom cloud in a quadrupole Ioffe configuration (QUIC) magnetic trap after a radio-frequency (RF) evaporative cooling of the trapped atom cloud. The *in-situ* absorption images of the atom cloud have shown clear bimodal optical density (OD) profiles which indicate the Bose–Einstein condensation (BEC) phase transition in the trapped gas. Also, we report here, for the first time, the measured variation in the sizes of the condensate and thermal clouds with the final frequency selected in the frequency scan of the RF-field for evaporative cooling. These results on frequency-dependent sizes of the clouds are consistent with the theoretical understanding of the BEC phenomenon in the trap.

Keywords. Laser atom cooling; magnetic trapping; evaporative cooling; Bose–Einstein condensation.

PACS Nos 37.10.Jk; 37.10.De; 67.85.−d; 52.55.Jd

1. Introduction

Over more than two decades, the laser atom cooling [1] and Bose–Einstein condensation (BEC) of dilute atomic gases [2,3] are under intense investigation for interesting physics as well as for various applications. With the advent of techniques of laser cooling and trapping of atoms, such as magneto-optical trap (MOT), an unprecedented control on the number and temperature in an atomic sample has been possible, which has proved useful in various atomic physics experiments [2,3] and technological applications such as atom lithography [4], accurate atomic clocks [5], cold-atom gyroscopes [6,7], cold-atom accelerometers and gravimeters [8], atomic magnetometers [9], etc. Cold atoms trapped in a periodic potential formed by the standing wave pattern of far detuned laser beams, known as optical lattice, mimic the electrons in a periodic potential of a crystal lattice. Because of the opportunity to tailor the potential of optical lattices in several ways, cold atoms and Bose condensate of atoms in optical lattices serve as test bed to model and verify various condensed matter phenomena with greater flexibility than before [10,11]. The cold atoms and Bose condensates in optical lattices also provide opportunity to explore several exciting dynamics of matter-waves in periodic potential [10,12,13]. These systems are also promising for future technology of quantum information processing [14]. The cooling and trapping of atoms has also enriched our basic understanding of atomic physics which includes behaviour of fermions and bosons confined in different dimensions and geometries, Feshbach resonances [15,16], dressed states of atoms in strong optical [17] and radio-frequency [18–20] fields.

Thus, preparation of cold atoms and Bose condensate of atoms is the first step to proceed towards their different uses as discussed above. A magneto-optical trap (MOT) is a robust and reliable technique to produce cold atomic samples in the temperature range of 10–100 μK with number density in the range of 10^{10}–10^{11} cm^{-3}. To obtain a Bose condensate of the atoms, for example in ^{87}Rb atom cloud, a further lower temperature (in the sub-micro-Kelvin range) and higher number density (in the range 10^{13}–10^{14} cm^{-3}) are needed. This comes from the requirement of the phase-space density ($\rho = n\lambda_{\mathrm{dB}}^3$) of the atom cloud to be greater than 2.61 for BEC, where n is the number density of atoms and λ_{dB} is the de Broglie wavelength.

Due to dissipative processes involved in resonant interaction of atoms with light, it is difficult to achieve such a high value of phase-space density in the atom cloud in a MOT. Thus, to achieve Bose–Einstein condensation (BEC) in a dilute atomic gas, the laser cooling in a MOT is used as the first stage of cooling which is succeeded by a second stage cooling, known as evaporative cooling [3,21–23]. Several variants of design of an experimental set-up are there to implement the above two-stage cooling protocol for achieving BEC. The second stage cooling, i.e. evaporative cooling, is performed while atoms are trapped in a conservative potential of either a magnetic trap or a dipole trap of a far-detuned laser beam [24]. An ultrahigh vacuum (UHV) environment is necessary to have a long lifetime of atoms in the trap during the evaporative cooling. This UHV requirement conflicts with the requirement of background vapour needed for the MOT loading. One way to resolve this issue is to use the concept of double-MOT set-up [25,26], in which the first MOT is formed in a vapour chamber and the second MOT is formed in an UHV chamber by transferring the cold atoms from the first MOT. The vapour chamber and UHV chamber are connected, but differentially pumped to maintain different levels of pressure. In the double-MOT set-up, the MOT in the vapour chamber is called 'VC-MOT', whereas the MOT in the UHV chamber is called 'UHV-MOT'. We have developed an experimental set-up based on this double-MOT concept, in which laser-cooled ^{87}Rb atoms are trapped in a magnetic trap and further cooled by RF field-induced evaporative cooling method, to achieve Bose–Einstein condensation (BEC) in the trapped atom cloud.

In this article, we report the details of our set-up and results of *in-situ* characterization of evaporatively cooled cloud of ^{87}Rb atoms in a quadrupole Ioffe configuration (QUIC) magnetic trap. The *in-situ* absorption images of the cooled atom cloud have shown clear bimodal optical density (OD) profiles which indicate the Bose–Einstein condensation (BEC) phase transition in the trapped atom cloud. We also report, for the first time to the best of our knowledge, the measured variation in the sizes of the condensate and thermal clouds with the final frequency chosen in the frequency scan of RF field used for evaporative cooling. The results are consistent with the theory. These *in-situ* results can be useful to characterize the Bose condensate when it is difficult to switch-off the trap for the time-of-flight observations.

This article is organized as follows. In §2, we discuss the double-MOT set-up developed for the realization of BEC of ^{87}Rb atoms in our lab. In this section, vacuum chambers for the formation of both the MOTs as well as for magnetic trapping, lasers and optical lay-out, coils used for MOT and magnetic traps and controller system for the set-up are discussed. In §3, the procedure for the formation of two MOTs, preparation of UHV-MOT cloud for magnetic trapping, magnetic trapping, evaporative cooling and characterization of cooled atom cloud by absorption probe imaging are discussed. Our main observations and results using the *in-situ* absorption imaging technique are presented in §4. The results show the evidence of BEC phase transition in the evaporatively cooled atom cloud, and sizes of the condensate and the thermal clouds are found to vary with the final frequency of RF field applied for evaporative cooling. Finally, we present the conclusions of this work in §5.

2. Experimental set-up

2.1 *Vacuum system*

The schematic of our experimental set-up for Bose–Einstein condensation of ^{87}Rb atoms is shown in figure 1. In this set-up, an octagonal chamber of stainless steel (SS) having rubidium (Rb) vapour at $\sim 2\times10^{-8}$ Torr pressure (pressure without vapour $\sim 1\times10^{-8}$ Torr) is used for the formation of vapour chamber MOT (VC-MOT). A quartz glass cell kept at a pressure of $\sim 5\times10^{-11}$ Torr, referred to as UHV-MOT chamber, is used for loading UHV-MOT. A narrow tube of length

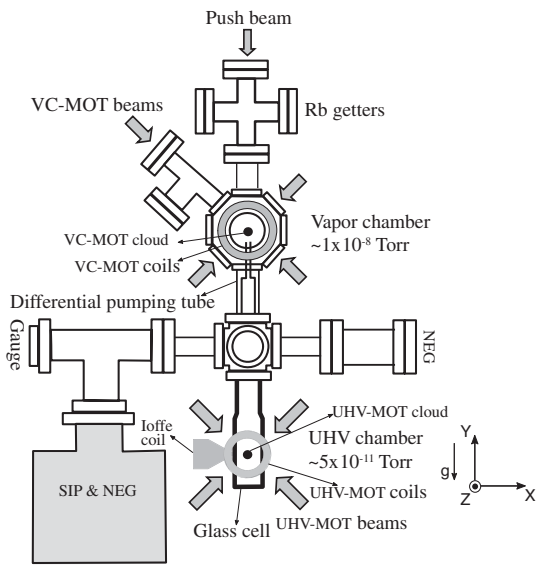

Figure 1. Schematic of the experimental set-up. SIP: sputter-ion pump and NEG: non-evaporable getter pump.

122 mm, called differential pumping tube (DPT), is connected between the cell and the octagonal chamber to ensure differential pressure between them. The upper part (towards the VC-MOT chamber) of this tube has a diameter of 2.5 mm, upto 60 mm length and the remaining part has a diameter of 5 mm. This design is adapted to achieve the desired conductance as well as to accommodate the transverse expansion of the atom flux during the transfer of atoms from VC-MOT to UHV-MOT. A six-way cross made from a cube of SS is used for connecting the octagonal VC-MOT chamber and the glass cell through the differential pumping tube, as shown in figure 1. The sides of this cube have appropriate knife edges to connect other components with NW35CF flanges. A combination sputter ion pump (VacIon plus, 150 l/s Starcell with a non-evaporable getter (NEG) module, from Varian, Italy) and a separate NEG pump (GP-100MK5, SORB-AC MK5-type cartridge pump from SAES getters, Italy) are also connected to the cube for pumping out the glass cell to the necessary UHV level. A turbomolecular pump (TMP) of 70 l/s capacity and a sputter ion pump of 20 l/s capacity are connected to the octagonal VC-MOT chamber. Bayerd–Alpert (BA)-type ion gauges are used for measuring the pressure in the VC-MOT chamber and glass cell during pumping. For measuring very low pressure in the glass cell (UHV-MOT chamber), an extractor gauge (Oerlikon Leybold), which can sense the pressure value upto 1×10^{-12} Torr, is connected to the chamber to which glass cell is connected. During the evacuation process, first the TMP is used for roughing and degassing of the whole vacuum system. A prolonged baking of the vacuum system for a week ($\sim 7 \times 24$ hours) at temperature 100–150°C is performed for a good degassing of the whole system. During this baking, all the ion pumps and gauges are also baked and degassed. After the vacuum system is cooled down, all the ion pumps and NEG modules are activated and then TMP is switched-off and isolated from the vacuum system by using a gate valve. With the ion pumps and NEG pumps ON, the pressure of $\sim 1 \times 10^{-8}$ Torr in the octagonal chamber and $\sim 5 \times 10^{-11}$ Torr in the glass cell is reached over a period of one to two days.

2.2 *Laser systems and optical lay-out*

The relevant energy levels of ^{87}Rb atom are shown in figure 2. The cooling transition for ^{87}Rb is $F = 2$ to $F' = 3$ and repumping transition is $F = 1$ to $F' = 2$. The frequencies of various laser beams used in the experiments are set as shown schematically in figure 2.

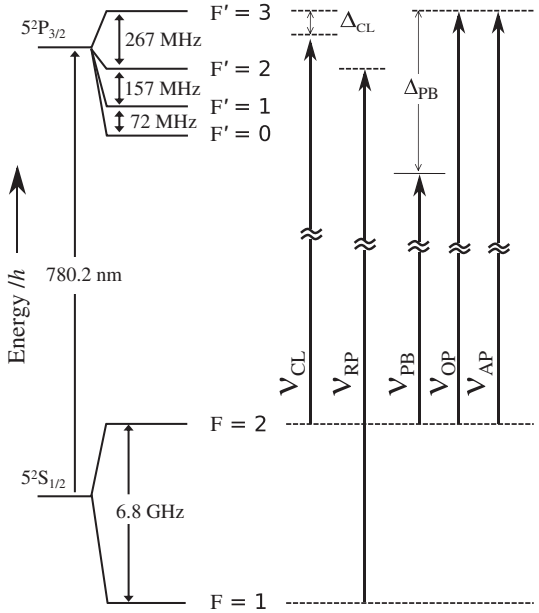

Figure 2. Schematic of the energy levels of ^{87}Rb atom relevant to laser cooling and BEC experiments. The frequencies and the corresponding detuning of various laser beams such as cooling (ν_{CL}), repumping (ν_{RP}), push (ν_{PB}), optical pumping (ν_{OP}) and absorption probe (ν_{AP}) are indicated.

Several external cavity diode laser (ECDL) systems, operating near $\lambda \sim 780.2$ nm, are used in the set-up, whose frequencies are stabilized and locked using saturated absorption spectroscopy (SAS) technique. The output laser beams from these lasers are used for cooling, repumping, pushing, optical pumping and absorption imaging purposes after appropriate adjustment of power, frequency and duration.

Figure 3 shows the schematic of the optical lay-out of the components used for manipulating the laser beams for various purposes. Various optical components such as polarizing beam splitters (PBSs), waveplates, mirrors, lenses, acousto-optic modulators (AOMs), beam expanders (BEs), etc., are used for different purposes which include splitting, combining, setting the polarization, reflecting, focussing, frequency shifting, switching or controlling power, expanding size, etc., of the laser beams. The cooling laser beams for VC-MOT and UHV-MOT are derived from the output beam from an amplifier TA (BoosTA, Toptica, Germany) which can deliver upto ~1500 mW power. This amplifier is seeded by an ECDL oscillator system (DL-100, TOPTICA, Germany, shown as DL-1 in figure 3) through a fibre coupling optics. The repumping laser beams for both the MOTs are obtained from two independent ECDL systems DL-2 and DL-3, capable of delivering ~150 mW and ~100 mW power

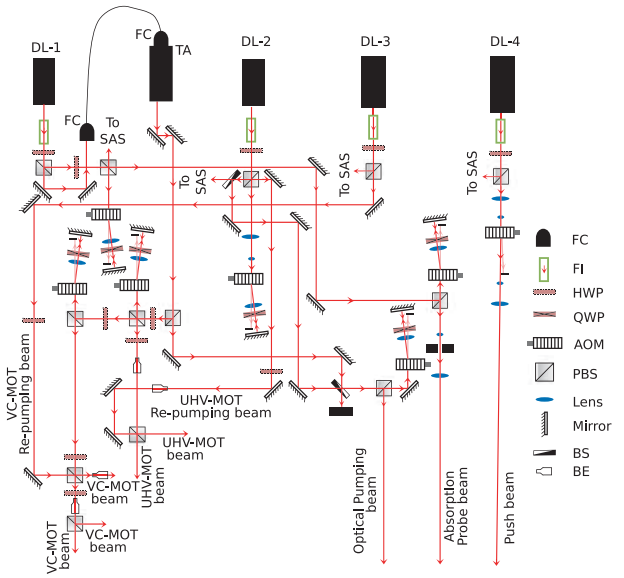

Figure 3. Schematic of the optical lay-out for the generation of various laser beams required for the formation of MOTs, optical pumping and absorption probe imaging. Various systems/components used in the set-up are abbreviated as FI: Faraday isolator, HWP: half waveplate, QWP: quarter waveplate, AOM: acusto-optics modulator, PBS: polarizing cube beam splitter, BS: beam splitter, FC: fibre coupling optics, BE: beam expander, DL-i (i=1 to 4): ECDL oscillators, TA: diode laser amplifier and SAS: saturated absorption spectroscopy.

respectively. The push beam is derived from another ECDL system DL-4 which can deliver upto ∼150 mW power. The absorption probe beam is derived from the cooling laser oscillator (DL-1), as shown in figure 3.

The output from the amplifier TA is split to obtain cooling beam for VC-MOT (power ∼250 mW), cooling beam for UHV-MOT (power ∼180 mW) and optical pumping beam (power ∼3 mW). The cooling beam for VC-MOT, after the double pass through an AOM, is further split and expanded to derive three VC-MOT beams (∼20 mW power in each beam). The VC-MOT re-pumping laser beam from the laser DL-3 (power ∼15 mW) is mixed to one of the three VC-MOT beams as shown in figure 3. These three VC-MOT beams are injected into the octagonal VC-MOT chamber through three viewports. The quarter waveplates are used to set appropriate polarization of the VC-MOT beams before entering into the chamber. These beams are retroreflected by the mirrors kept at the other end of the chamber near the exit viewports, to get the six beams required for the VC-MOT. Before each retroreflecting mirror, a quarter waveplate is placed to ensure appropriate polarization of a retroreflected beam entering the chamber for the formation of VC-MOT. The cooling beam for UHV-MOT, after the double pass through an AOM and expansion, is first mixed with a re-pumping laser beam and then split to obtain two UHV-MOT beams as shown in figure 3. The repumping beam for UHV-MOT is derived from DL-2 laser after the double pass through an AOM as shown in figure 3. These two UHV-MOT beams are further split to obtain six independent UHV-MOT beams. All the six UHV-MOT beams have nearly equal power (∼10 mW in each beam) in the cooling laser part. However, the repumping power (total ∼20 mW in six beams) is not equally distributed in all the six UHV-MOT beams. This is because when cooling and repumping beams are combined on a PBS, the polarizations of cooling and re-pumping parts are different in the combined beam. A further splitting of such a combined beam is expected to result in different ratios of cooling and repumping powers in different beams. We deliberately keep the cooling laser power equal in all the six UHV-MOT beams, as different repumping laser power in these UHV-MOT beams does not cause any problem in the operation of UHV-MOT. The equal cooling power in all the six beam is helpful in achieving the stable UHV-MOT atom cloud, as well as for lowering the atom cloud temperature in the molasses stage.

2.3 *Coils for MOTs and magnetic trap*

For the VC-MOT, a pair of nearly identical coils having currents in anti-Helmholtz configuration is used. Each coil has 150 number of turns of copper wire of diameter ∼1.5 mm, with size of each coil as: inner diameter (ID) ∼57 mm, external diameter (ED) ∼66 mm and length ∼38 mm. The coils provide a quadrupole field gradient of ∼10 G/cm in the axial direction at 3 A current in the coils for ∼55 mm face-to-face separation between the coils. For the UHV-MOT, another pair of coils, each coil having 230 number of turns (ID ∼ 34 mm, ED ∼ 70 mm, length ∼ 35 mm and wire diameter ∼ 1.4 mm), is used with ∼47 mm face-to-face separation between the coils. With the current in anti-Helmholtz configuration, these coils generate quadrupole field with an axial field gradient of ∼10 G/cm for 1 A of current in each coil. These UHV-MOT coils are also used as quadrupole trap coils for the magnetic trapping of the atoms after initial cooling and trapping of atoms in the UHV-MOT. In the quadrupole magnetic trap, a high current (>20 A) flows in the coils, because of which the cooling of the coils is necessary. Therefore, these coils are kept inside the Teflon housing in

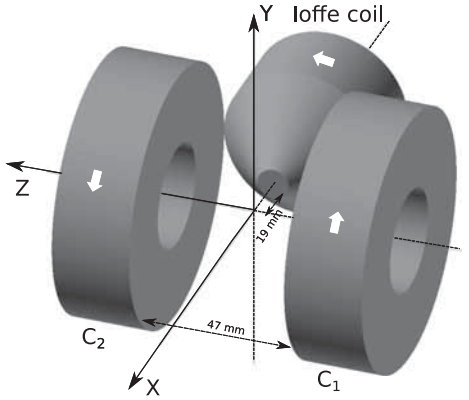

Figure 4. Schematic of the coils arranged for a QUIC trap. The coils C_1 and C_2 denote the quadrupole trap coils. The coordinate axes and relative positions of the coils used in the set-up are shown. White arrows show the directions of the current in different coils.

which cold water is circulated for cooling the coils during the operation of the magnetic trap. The quadrupole magnetic trap is converted into a quadrupole Ioffe configuration (QUIC) trap by including a third coil (called Ioffe coil) in the quadrupole trap set-up. In the QUIC trap, a non-zero magnetic field at the minimum of the trapping potential is achieved, which helps in reducing trap losses due to Majorana spin flips encountered in a quadrupole trap [27]. The Ioffe coil is placed at an axis passing through the quadrupole trap centre and perpendicular to the quadrupole trap axis, as shown in figure 4. In our QUIC trap, the Ioffe coil has 238 number of turns (with 78 number of turns in the conical part and 160 number of turns in the cylindrical part). The conical section of the Ioffe coil has a length of 16 mm with gradually increasing diameter (from 6 mm to 35 mm) and the cylindrical section is of 18 mm length with 35 mm diameter. The wire used in this coil has ∼1.0 mm diameter. This specific conical design of the Ioffe coil is chosen so that the coil can approach the glass cell without blocking the UHV-MOT beams.

2.4 *Controller system*

An industrial personal computer (PC) installed with a field programmable gate array (FPGA) card has been used to program and control the experimental procedure in the desired sequence. The durations and sequence of various events from VC-MOT formation to evaporative cooling and imaging are set using this controller system. The FPGA card is provided control through LabVIEW program. The generated signals from FPGA are appropriately amplified and used as trigger signals to various electronic devices such as power supplies, AOMs, mechanical shutters, CCD cameras, RF synthesizers and other circuitries. For switching-ON the current in the quadrupole trap coils, an insulated gate bipolar transistor (IGBT)-based switching circuitry is used, which results in a rise-time of ∼2.5 ms to reach the required current in the coils. This circuitry also works after receiving an appropriate trigger pulse from the controller system.

3. Experimental procedure

In the experiments, the first event is the formation of VC-MOT. Then, a push laser beam is focussed on the VC-MOT atom cloud to eject atoms from this MOT. The atoms ejected from the VC-MOT pass through the differential pumping tube (DPT) (figure 1) and reach the glass cell where they are recaptured in the UHV-MOT. The atoms in the UHV-MOT undergo various processes such as the MOT compression, optical molasses and optical pumping, before being trapped in the magnetic trap for evaporative cooling. A summary of all these events and processes during the experiments is presented in the following parts of this section.

3.1 *VC-MOT formation*

The VC-MOT is loaded from the background Rb-vapour in the octagonal chamber (figure 1). The Rb vapour is generated in this chamber by passing a direct current of 2.7–3.5 A in the Rb-getter strips resulting in a background vapour pressure of $\sim 2 \times 10^{-8}$ Torr for MOT formation. The Rb-getter strips are fixed on a feed-through and inserted inside the chamber by mounting this feed-through on one of the ports of the octagonal VC-MOT chamber. The VC-MOT beams are injected in the chamber as described in §2.2. A direct current of ∼3 A is passed through the VC-MOT coils to generate the required magnetic field gradient of ∼12 G/cm for the MOT formation. The cooling laser frequency is locked at a side of the cooling transition (with red detuning of ∼13 MHz) whereas re-pumping laser frequency is kept at the resonance to the re-pumping transition of the ^{87}Rb atom. In our VC-MOT, we could trap $\sim 1 \times 10^8$ ^{87}Rb atoms at ∼300 μK temperature.

3.2 *Atom transfer and UHV-MOT formation*

The atoms cooled and trapped in the VC-MOT are utilized for loading the UHV-MOT in the glass cell.

The VC-MOT and UHV-MOT are separated by a distance of ∼360 mm in our set-up. The transfer of atoms from the VC-MOT to the UHV region in the glass cell, through the narrow differential pumping tube (DPT), is an important step in loading the UHV-MOT. This atom transfer from VC-MOT to UHV-MOT has been studied in detail by several groups [26,28–35] to increase the number of atoms in UHV-MOT. The use of a red-detuned (from cooling transition of ^{87}Rb) push laser beam of Gaussian transverse profile is a very convenient method to transfer atoms from the VC-MOT to the UHV-MOT. This red-detuned push beam ejects the atoms from the VC-MOT and also provides a transverse confinement (i.e. guiding) to the atoms during their travel from VC-MOT to UHV-MOT. This guiding facilitates more number of atoms reaching the UHV-MOT region and hence enhances the number of atoms in the UHV-MOT. In our experiments, a laser beam having ∼21 mW of power (before entering into the VC-MOT chamber) and detuning ∼1 GHz, focussed to a $1/e^2$ radius of ∼35 μm on VC-MOT atom cloud, is used as a push beam for atom transfer. During the UHV-MOT loading, UHV-MOT beams are kept ON and appropriate current (∼0.6–1.0 A) is passed through the UHV-MOT coils to generate the necessary field gradient for the MOT formation. In our experiments, the UHV-MOT is fully loaded in ∼40 s duration when the push beam is focussed on the VC-MOT atom cloud. Nearly $\sim 2\times 10^8$ atoms are obtained in the saturated UHV-MOT in our experiments. The temperature of the atom cloud in the UHV-MOT ranges from 100 μK to 400 μK, depending upon the values of various experimental parameters. The number and temperature of the atom clouds in both the MOTs are estimated by fluorescence imaging and free-expansion techniques [26,31].

3.3 *Preparation of UHV-MOT atom cloud for magnetic trapping*

For trapping an atom cloud from a MOT in a magnetic trap efficiently, the lowering of the temperature of the cloud and transferring the atoms to a trappable Zeeman state is required. For this purpose, the atom cloud from the UHV-MOT is first kept in a compressed MOT (for ∼20 ms), which leads to increased density and reduced size of the cloud. The compressed MOT is formed by increasing the detuning of the cooling UHV-MOT beams from −13 MHz to −25 MHz and magnetic field gradient from 6 G/cm to 8 G/cm. At the end of the compressed MOT stage, the current in the UHV-MOT coils is switched-off and atoms are cooled in optical molasses for ∼5 ms. In the molasses, the cooling laser beams are kept at five times lower power than the UHV-MOT beams at increased detuning to ∼42 MHz. After the optical molasses stage the temperature of atom cloud is in the range of ∼40–80 μK.

The atom cloud, after cooling in molasses, is optically pumped to ($F = 2, m_F = 2$) Zeeman hyperfine sublevel of ^{87}Rb atom, which is suitable for magnetic trapping. The optical pumping is accomplished in ∼0.5 ms, in which the atom cloud from the molasses is exposed to a weak laser pulse (with σ^+ polarization) of ∼0.5 ms duration in the presence of a uniform magnetic field of ∼2 G. We have optimized the optical pumping by varying the power in the optical pumping pulse while keeping the pulse duration fixed at ∼0.5 ms. At an optimized optical pumping power (∼250 μW), we could transfer ∼30–40% of atoms from UHV-MOT to the quadrupole magnetic trap. The number of atoms transferred to the magnetic trap can be further increased by improving the optical pumping as well as by improving the rise time of the current in the quadrupole trap coils.

3.4 *Magnetic trapping*

In magnetic trapping, the optically pumped atom cloud is first trapped in the quadrupole trap by switching on (in ∼2.5 ms) a current I_q ∼13 A in the quadrupole coils, which is then slowly increased to I_q ∼ 23 A in ∼1 s duration. This quadrupole trap is then converted to a QUIC trap by increasing the Ioffe coil current (I_{Ioffe}) from 0 A to ∼19.5 A slowly in ∼2.5 s duration. The calculated fields due to quadrupole and Ioffe coils are shown in figure 5 for the geometrical arrangements of coils shown in figure 4. From the graphs in figure 5, it is evident that Ioffe configuration [27] in the QUIC trap is achieved at $I_q = 23$ A and $I_{Ioffe} = 19.5$ A. Our measured magnetic field values are close to these calculated values.

The trapping potential for the QUIC trap in the vicinity of the minimum field position (i.e. $x = -x_0$ on the x-axis) can be approximately written as [36–38]

$$U(r) = \mu |B(\mathbf{r})| = \mu B_0 + \frac{m}{2}(\omega_\parallel^2 (x+x_0)^2 + \omega_\perp^2 (y^2+z^2)), \quad (1)$$

where m is the mass of the atom, μ is the magnetic dipole moment of the atom and B_0 is the non-zero value of the magnetic field at the field minimum position x_0. The frequencies

$$\omega_\parallel = \sqrt{\frac{\mu B_x''}{m}}$$

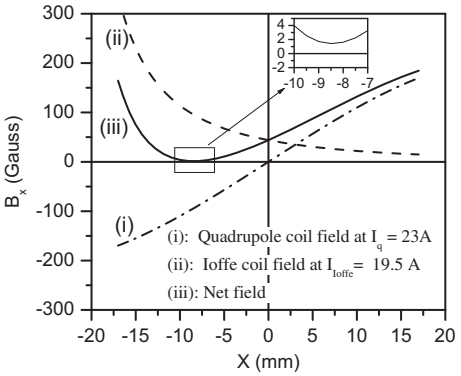

Figure 5. Variation of magnetic field with position along the x-axis (Ioffe-coil axis) due to different coils in the QUIC trap. The inset shows the expanded plot near the minimum of the magnetic field with $B_0 = 1.4$ G at $x = -8.5$ mm $(= -x_0)$.

and

$$\omega_\perp = \sqrt{\frac{\mu B_\perp'^2}{m B_0}}$$

are axial and radial trap frequencies for QUIC trap, where B_x'' is the curvature of the field along the x-axis (Ioffe coil axis) and $B_\perp' = \sqrt{B_y' B_z'}$ is the geometric mean of the field gradients B_y' and B_z'. For ($F = 2$, $m_F = 2$) Zeeman hyperfine sublevel of ^{87}Rb atom, $\sqrt{\mu/m} = 2\pi \times 1.2765$, which gives the axial and radial trap frequencies for our QUIC trap as $\omega_\parallel(\text{Hz}) = 2\pi \times 1.2765\sqrt{B_x''(\text{G/cm}^2)}$ and $\omega_\perp(\text{Hz}) = 2\pi \times 1.2765\sqrt{(B_\perp'^2/B_0)(\text{G/cm}^2)}$ respectively. For $I_q = 23$ A and $I_{\text{Ioffe}} = 19.5$ A, the trap frequencies are $\omega_\parallel = 2\pi \times 17.6$ Hz and $\omega_\perp = 2\pi \times 174.2$ Hz (with $\omega_y = 2\pi \times 122.5$ Hz and $\omega_z = 2\pi \times 246$ Hz).

It is known that during the conversion of quadrupole trap to QUIC trap, depending upon the value of current in the Ioffe coil (I_{Ioffe}), the minimum of the magnetic field (and potential) gets shifted from the quadrupole trap centre ($x = y = z = 0$) to a new position towards the Ioffe coil [27]. This results in I_{Ioffe}-dependent shift in the position of the trapped atom cloud towards the Ioffe coil. Figure 6 shows (absorption images, discussed later) the observed shift in the position of trapped atom cloud in our experiments for different values of I_{Ioffe} and a fixed value of $I_q = 23$ A. Each of these images was captured after running a fresh cycle of trapping experiment (from VC-MOT formation to magnetic trapping), including the ramping of the Ioffe coil current from zero to the set value I_{Ioffe}. The image of the atom cloud was captured after the Ioffe coil current reached the set value. For a set value of

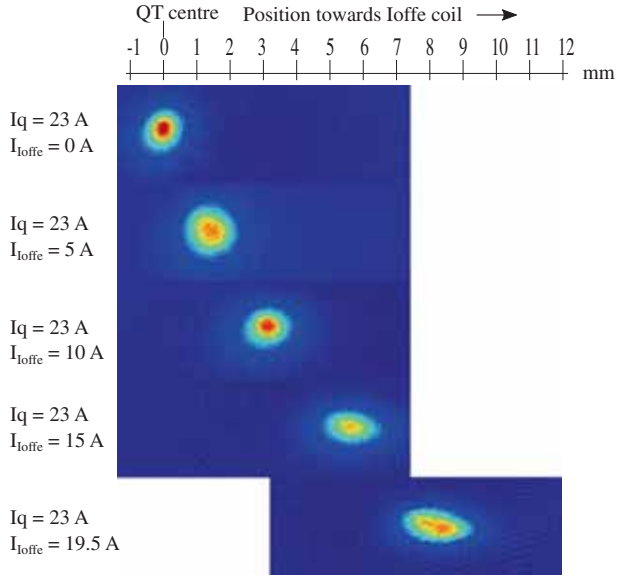

Figure 6. Absorption images of the trapped atom cloud showing the shift in the position of the cloud with increase in the Ioffe coil current. For the last image in the figure, the components of the imaging set-up (i.e. probe beam, optics and CCD camera) were translated to bring the cloud image in the centre of the CCD camera. The colours from blue to red in the OD images show OD values in the increasing order.

$I_{\text{Ioffe}} = 19.5$ A (with $I_q = 23$ A), the observed shift in the atom cloud position was ~8.5 mm, which is in good agreement with the calculated value of $x_0 = 8.5$ mm for the magnetic field minimum (shown in figure 5). This evidently shows the appropriate working of the QUIC trap in our experiments.

A longer lifetime of the atom cloud in the magnetic trap is always helpful for evaporative cooling. Several factors such as the vacuum level in the trap chamber, the light going into the trap region during magnetic trapping, etc. affect this lifetime. During the magnetic trapping of atoms, it is important to tackle these issues. We have used mechanical shutters at different places to block the leaked radiation from AOMs during magnetic trapping and evaporative cooling. Also, the trapping region is isolated by putting a physical partition on the table and maintaining darkness in the trapping region. With all these precautions and $\sim 5 \times 10^{-11}$ Torr pressure in the trapping chamber (glass cell), we get a lifetime of ~20 s for atom cloud in our QUIC trap.

3.5 *RF evaporative cooling*

In radio-frequency (RF) evaporative cooling, RF field is used to force the ejection of hotter atoms from the trapped atom cloud so that remaining cloud is settled

to a lower temperature after the thermalization process [39,40]. For evaporative cooling of ^{87}Rb atoms trapped in our QUIC trap, we apply RF radiation emitted from a single-loop antenna kept at one side of the glass cell with its axis aligned along the quadrupole trap axis (z-axis). We use a programmable synthesizer (Agilent 55332A) as an RF source whose output is connected to an RF amplifier. The antenna is connected to this RF amplifier output through an impedance-matching circuit. For evaporative cooling, frequency of the RF radiation is scanned from higher initial value to a lower final value (called RF scan), employing a logarithmic variation of frequency with time [41]. This kind of RF scan results in an efficient evaporative cooling process [3]. The useful frequency range for the RF scan can be estimated by knowing the spatial variation of the trap magnetic field and the size of the atom cloud in the trap. The parameters of the atom cloud after RF evaporation are sensitive to the value of final frequency in the RF scan.

3.6 *Absorption probe imaging and image analysis*

We have used the well-known absorption probe imaging method [3] to characterize the atom cloud in the magnetic trap. In absorption probe technique, the atom cloud is illuminated by a low-intensity resonant probe laser pulse (duration ~60 μs) propagating along z-axis in our set-up. The absorption shadow of the atom cloud is imaged onto a charged coupled device (CCD) camera using an appropriate optics. In the experiments, we acquire three images to get the required information: (i) the background image which is obtained without absorption probe beam (IBG), (ii) the image of the probe beam without atom cloud (IP) and (iii) the image of the probe beam transmitted through the atom cloud (IT). From these three images and using an image processing program, we construct the optical density (OD) image of the atom cloud using the following equation:

$$\mathrm{OD}(i,j) = \ln \frac{\mathrm{IP}(i,j) - \mathrm{IBG}(i,j)}{\mathrm{IT}(i,j) - \mathrm{IBG}(i,j)}, \qquad (2)$$

where (i, j) denote the pixel position at the CCD element in the acquired images. This OD image gives the column density of the atom cloud as $\mathrm{OD}(x, y) = \int(\sigma_0 \cdot n(x, y, z)\mathrm{d}z)$, where σ_0 is the absorption cross-section and $n(x, y, z)$ is the density of the atom cloud. The plot of $\mathrm{OD}(x, y)$ gives important information about the atom cloud, which include the transverse distribution of column density, width, etc.

4. Results and discussion

After the completion of RF scan, the evaporatively cooled atom cloud is characterized by *in-situ* absorption imaging method as discussed before. The images of evaporatively cooled cloud are recorded for different frequency ranges in RF scan. As absorption imaging is a destructive technique which modifies the cloud parameters, we have to reload the magnetic trap and perform evaporative cooling again to observe the effect of any modification in trapping and evaporative cooling parameters on the cooled atom cloud. Because of the several steps involved in a complete cycle of evaporative cooling experiment, the recorded images show some cycle-to-cycle fluctuation in the number of cooled atoms (±10%) even at a fixed set of experimental parameters. The evaporative cooling experiments are performed over a number of cycles to record the absorption images for different ranges of RF scan.

Figure 7 shows the OD images and spatial profiles of the evaporatively cooled atom cloud for different ranges of RF scan. The power of RF field was ~6–8 W over these ranges. For some of the RF scan ranges, the spatial profile of OD becomes bimodal (as shown in figure 7), with a sharp peak at the centre against a broad Gaussian distribution at the skirts. This bimodal

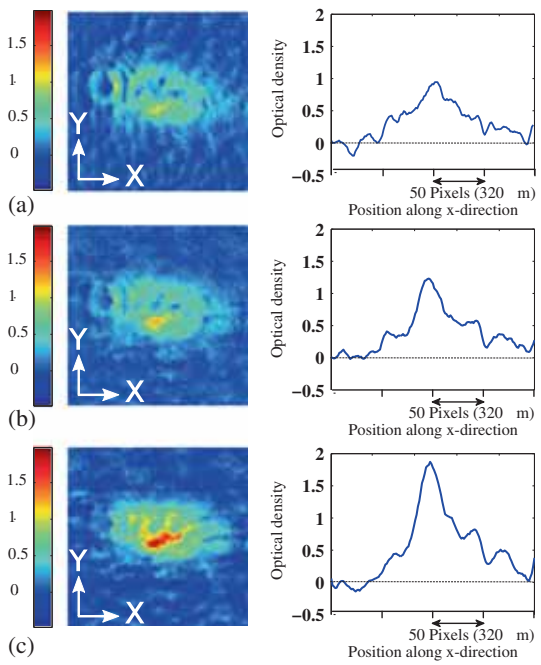

Figure 7. OD images and spatial profiles of the atom cloud cooled by RF evaporation for different scan ranges of frequency. (**a**) 20 MHz–2.5 MHz, (**b**) 20 MHz–2.3 MHz and (**c**) 20 MHz–2.2 MHz. The colours from blue to red in the OD images show OD values in the increasing order.

distribution indicates the onset of Bose–Einstein condensation of atoms at the trap centre. This kind of bimodal distribution in OD profile is a well-known signature of the occurrence of BEC during the evaporative cooling experiments [42]. We note that the bimodal spatial profile of OD is observable only for appropriately chosen parameters during the RF evaporation experiments. The bimodal distribution obtained in the OD profile of the cooled atom cloud is quite sensitive to the final value of frequency in the RF scan.

The total number N can be estimated by summing the column density values in the recorded OD image. The column density with a bimodal profile, having both condensate and thermal cloud, can be written as [43]

$$\tilde{n}(x,y) = \tilde{n}_{\mathrm{c}} \max\left(1-\left(\frac{x-x_0}{w_x/2}\right)^2-\left(\frac{y-y_0}{w_y/2}\right)^2, 0\right)^{3/2} + \tilde{n}_{\mathrm{th}} \exp\left[-\frac{(x-x_0)^2}{2(\sigma_x/2)^2}-\frac{(y-y_0)^2}{2(\sigma_y/2)^2}\right], \quad (3)$$

where $\tilde{n}_{\mathrm{th}}$ and $\tilde{n}_{\mathrm{c}}$ are the peak column density values for the thermal and the condensate clouds, and σ_x, σ_y, w_x and w_y are width parameters for the thermal and the condensate parts of the cloud. The temperature (T) and chemical potential (μ) can be estimated by fitting the observed OD profile to eq. (3) and using the relations $k_{\mathrm{B}}T = \frac{1}{4}m\omega_x^2\sigma_x^2$ and $\mu = \frac{1}{8}m\omega_x^2 w_x^2$ as discussed in ref. [43], where k_{B} is the Boltzmann's constant. A typical fit is shown in figure 8. For an image shown in figure 7c, these parameters are estimated as $T \sim 3.2\ \mu$K, $\mu \sim 440\ n$K and $N \sim 6 \times 10^5$.

In the OD images in which bimodal distribution is prominent, a halo surrounding the peak of OD is observed. This halo region has negative OD values (figure 9), implying that light intensity in this region in the probe beam image with atom cloud is higher than the intensity in the probe image without atom cloud. Similar halo region has been reported earlier [44,45] and attributed to the diffraction of probe beam from the dense and spatially localized Bose condensate cloud [44]. The OD image profiles which do not show bimodal distribution have negligible negative OD (as evident from figure 9).

It is known that the size of the cloud in the magnetic trap is dependent on its temperature [43,46]. Since the temperature of evaporatively cooled atom cloud is also dependent on the final value of RF frequency in the RF scan [43,45], we attempted to study the variation in the size of the cooled atom cloud with the value of the final frequency in the RF scan. Figure 10 shows the observed variation in the sizes of the thermal and condensate clouds with the value of final frequency in the RF scan. Here sizes were estimated by fitting eq. (3) to the measured OD profiles of the cooled atom cloud. An example of the fitting is shown in figure 8. The data in figure 10 show the decrease in the size of the thermal cloud with decrease in the final frequency, before the appearance of the bimodal OD profile. When final frequency is reduced below a certain value, the OD profile becomes bimodal. We observe that at the onset of bimodal distribution, the size of the condensate part is much smaller than the thermal part (figure 7). This is consistent with the prediction of sudden decrease in the size of the cloud below the critical temperature [46,47].

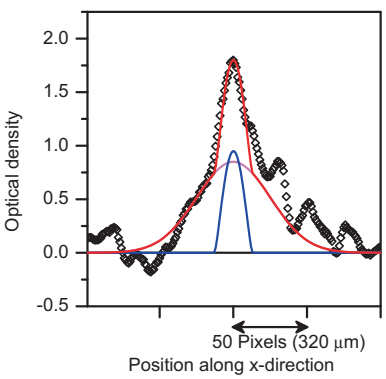

Figure 8. Measured optical density (OD) profile (diamonds) along the x-axis and its fits to eq. (3) for thermal (pink curve) and Bose condensate (blue curve) parts of the cloud. The red curve shows the resultant fit.

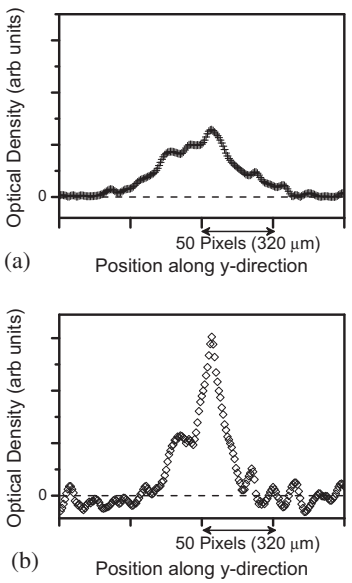

Figure 9. Optical density profile along y-direction. (**a**) Pure thermal cloud and (**b**) thermal cloud with condensate. The profile is shown in y-direction in which condensate is tightly confined in the QUIC trap. The profile in (**b**) shows more negative OD values (i.e. presence of halo) compared to the profile in (**a**).

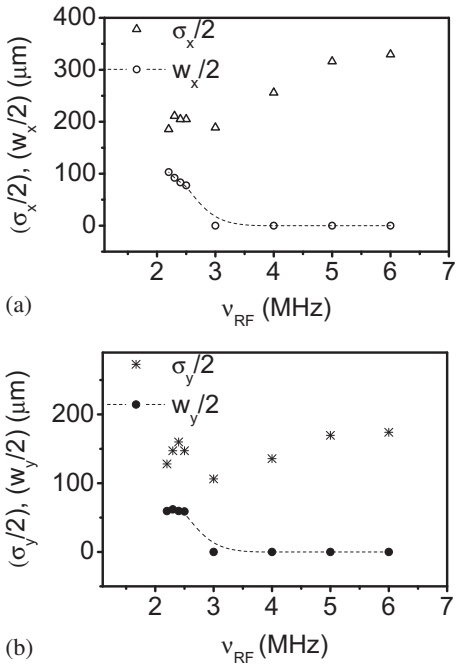

Figure 10. Measured variation in the cloud sizes along x- and y-directions with final frequency (ν_{RF}) in the RF scan. The scan range was from 20 MHz to ν_{RF}.

Figure 10a shows that when condensate part appears in the OD profile, the condensate size starts increasing with decrease in the final frequency in the RF scan. This increase in the condensate size can be attributed to the increased repulsive interactions with increase in the number of atoms in the condensate cloud, as has been discussed in ref. [46]. We note that increase in the condensate width with decrease in the final frequency in RF scan is more clearly observable along the weakly confining trap axis (i.e. x-axis), as compared to the strongly confining y-axis. Further, as we observed in our experiments (figure 10), in the presence of the condensate, the size of the thermal cloud also increases with decrease in the final frequency. This is consistent with the predictions made earlier [46,48] that the presence of the condensate pushes the thermal cloud out. Thus, our size-dependent observations shown in figure 10 are consistent with the theoretical understanding about BEC in the trap.

5. Conclusion

We have presented the generation and characterization of the Bose condensate of ^{87}Rb atoms in our home-made experimental set-up. The finally cooled atom cloud in the QUIC trap has been characterized by *in-situ* absorption imaging technique. The observed bimodal spatial profiles of optical density are suggestive of the presence of Bose condensate in the trap. We have observed variation in the sizes of condensate and thermal clouds with the final frequency in the frequency scan of the RF-field used for evaporative cooling. These results on frequency-dependent sizes of the condensate and thermal clouds are consistent with the theory of BEC in the trap.

Acknowledgement

The authors would like to thank V B Tiwari, S Singh, V Singh, A Srivastava and A Chakraborty for their help in the experiments. They are also thankful to V Bhanage, P P Deshpande, S Tiwari, L Jain and A Pathak for developing the controller system, C Rajan and P Kumar for developing the switching circuitry, M Lad and P S Bagduwal for providing the RF amplifier, H S Vora for image processing software, K V A N P S Kumar and S K Shukla for help in the vacuum system.

References

[1] C S Adams and E Riis, *Prog. Quantum. Electron.* **21**, 1 (1997), ISSN 0079-6727, http://www.sciencedirect.com/cience/article/pii/S0079672796000067
[2] M H Anderson, J R Ensher, M R Matthews, C E Wieman and E A Cornell, *Science* **269**, 198 (1995), http://www.sciencemag.org/content/269/5221/198.full.pdf, http://www.sciencemag.org/content/269/5221/198.abstract
[3] *Proceedings of the International School of Physics, Enrico Fermi Course CXL*, edited by M Inguscio, S Stringari and C E Wieman (IOS Press, Amsterdam, 1999)
[4] C O Dwyer, G Gay, B V de Lesegno, J Weiner, A Camposeo, F Tantussi, F Fuso, M Allegrini and E Arimondo, *Nanotechnology* **16**, 1536 (2005), http://stacks.iop.org/0957-4484/16/i=9/a=022
[5] A D Ludlow, M M Boyd, J Ye, E Peik and P O Schmidt, *Rev. Mod. Phys.* **87**, 637 (2015), DOI: 10.1103/RevModPhys.87.637
[6] A Gauguet, B Canuel, T Lévèque, W Chaibi and A Landragin, *Phys. Rev. A* **80**, 063604 (2009), DOI: 10.1103/PhysRevA.80.063604
[7] J Fang and J Qin, *Sensors* **12**, 6331 (2012), ISSN 1424-8220, http://www.mdpi.com/1424-8220/12/5/6331
[8] Q Bodart, S Merlet, N Malossi, F P Dos Santos, P Bouyer and A Landragin, *Appl. Phys. Lett.* **96**, 134101 (2010), http://scitation.aip.org/content/aip/journal/apl/96/13/10.1063/1.3373917
[9] N Behbood, F Martin Ciurana, G Colangelo, M Napolitano, M W Mitchell and R J Sewell, *Appl. Phys. Lett.* **102**, 173504 (2013), http://scitation.aip.org/content/aip/journal/apl/102/17/10.1063/1.4803684
[10] M Lewenstein, A Sanpera, V Ahufinger, B Damski, A Sen(De) and U Sen, *Adv. Phys.* **56**, 243 (2007), DOI: 10.1080/00018730701223200
[11] M Inguscio and L Fallani, *Atomic physics*: *Precise measurements and ultracold matter* (Oxford University Press Inc, New York, 2013)

[12] O Morsch and M Oberthaler, *Rev. Mod. Phys.* **78**, 179 (2006), DOI: 10.1103/RevModPhys.78.179
[13] I Bloch, J Dalibard and W Zwerger, *Rev. Mod. Phys.* **80**, 885 (2008) (since 1996) 1892
[14] I Bloch, J Dalibard and S Nascimbene, *Nat. Phys.* **8**, 267 (2012), ISSN 1745-2473, DOI: 10.1038/nphys2259
[15] S Inouye, M R Andrews, J Stenger, H-J Miesner, D M Stamper- Kurn and W Ketterle, *Nature* **392**, 151 (1998), ISSN 0028-0836, DOI: 10.1038/32354
[16] C Chin, R Grimm, P Julienne and E Tiesinga, *Rev. Mod. Phys.* **82**, 1225 (2010), DOI: 10.1103/RevModPhys.82.1225
[17] C Cohen-Tannoudji and D Guéry-Odelin, *Advances in atomic physics*: *An overview* (World Scientific Publishing Co. Ltd., Singapore, 2011)
[18] O Zobay and B M Garraway, *Phys. Rev. Lett.* **86**, 1195 (2001), DOI: 10.1103/PhysRevLett.86.1195
[19] O Morizot, Y Colombe, V Lorent, H Perrin and B M Garraway, *Phys. Rev. A* **74**, 023617 (2006), DOI: 10.1103/PhysRevA.74.023617
[20] A Chakraborty, S R Mishra, S P Ram, S K Tiwari and H S Rawat, *J. Phys. B* **49**, 075304 (2016), http://stacks.iop.org/0953-4075/49/i=7/a=075304
[21] H F Hess, *Phys. Rev. B* **34**, 3476 (1986)
[22] W Ketterle and N V Druten, Advances in atomic, molecular, and optical physics (Academic Press, 1996) Vol. 37, pp. 181–236, http://www.sciencedirect.com/science/article/pii/S1049250X08601019
[23] M H Anderson, J R Ensher, M R Matthews, C E Wieman and E A Cornell, in: *Laser Spectroscopy, XII International Conference* edited by M Inguscio, M Allegrini and A Sasso (World Scientific, 1995) p. 3
[24] M D Barrett, J A Sauer and M S Chapman, *Phys. Rev. Lett.* **87**, 010404 (2001), DOI: 10.1103/PhysRevLett.87.010404
[25] C J Myatt, N R Newbury, R W Ghrist, S Loutzenhiser and C E Wieman, *Opt. Lett.* **21**, 290 (1996)
[26] S R Mishra, S P Ram, S K Tiwari and S C Mehendale, *Phys. Rev. A* **77**, 065402 (2008)
[27] T Esslinger, I Bloch and T W Hänsch, *Phys. Rev. A* **58**, R2664 (1998)
[28] S P Ram, S K Tiwari and S R Mishra, *J. Korean Phys. Soc.* **57**, 1303 (2010)
[29] S P Ram, S R Mishra, S K Tiwari and S C Mehendale, *Rev. Sci. Instrum.* **82**, 126108 (2011), http://link.aip.org/link/?RSI/82/126108/1
[30] S P Ram, S K Tiwari, S R Mishra and H S Rawat, *Rev. Sci. Instrum.* **84**, 073102 (2013), http://link.aip.org/link/?RSI/84/073102/1
[31] S P Ram, *Studies on generation and manipulation of laser cooled atoms*, Ph.D. thesis (Homi Bhabha National Institute, 2013)
[32] J Wang, J Wang, S Yan, T Geng and T Zhang, *Rev. Sci. Instrum.* **79**, 123116 (2008)
[33] Y Shu-Bin, G Tao, Z Tian-Cai and W Jun-Min, *Chin. Phys.* **15**, 1746 (2006), http://stacks.iop.org/1009-1963/15/i=8/a=019
[34] E Dimova, O Morizot, G Stern, C G Alzar, A Fioretti, V Lorent, D Comparat, H Perrin and P Pillet, *Eur. Phys. J. D* **42**, 299 (2007)
[35] T B Swanson, D Asgeirsson, J A Behr, A Gorelov and D Melconian, *J. Opt. Soc. Am. B* **15**, 2641 (1998)
[36] T P Meyrath, *Experiments with Bose–Einstein condensation in an optical box*, Ph.D. thesis (University of Texas at Austin, 2005)
[37] M S Yoon, *Experiments on magnetic transport, magnetic trapping and Bose–Einstein condensation*, Ph.D. thesis (University of Oxford, 2009)
[38] J-F Schaff, P Capuzzi, G Labeyrie and P Vignolo, *New J. Phys.* **13**, 113017 (2011), http://stacks.iop.org/1367-2630/13/i=11/a=113017
[39] W Petrich, M H Anderson, J R Ensher and E A Cornell, *Phys. Rev. Lett.* **74**, 3352 (1995), DOI: 10.1103/PhysRevLett.74.3352
[40] D E Pritchard, *Phys. Rev. Lett.* **51**, 1336 (1983)
[41] B Lu and W A van Wijngaarden, *Can. J. Phys.* **82**, 81 (2004)
[42] W Ketterle, D S Durfee and D M Stamper-Kurn, in: *Proceedings of the International School of Physics – Enrico Fermi* edited by M Inguscio, S Stringari and C E Wieman (IOS Press, 1999) p. 67
[43] D M Stamper-Kurn, H-J Miesner, S Inouye, M R Andrews and W Ketterle, *Phys. Rev. Lett.* **81**, 500 (1998), DOI: 10.1103/PhysRevLett.81.500
[44] C C Bradley, C A Sackett, J J Tollett and R G Hulet, *Phys. Rev. Lett.* **75**, 1687 (1995), *ibid*. **79**, 1170 (1997)
[45] W Yu-Zhu, Z Shu-Yu, L Quan, Z Shan-Yu and F Hai-Xiang, *Chin. Phys. Lett.* **20**, 799 (2003), http://stacks.iop.org/0256-307X/20/i=6/a=306
[46] W Zhang, Z Xu and L You, *Phys. Rev. A* **72**, 053627 (2005), doi: 10.1103/PhysRevA.72.053627
[47] D S Durfee and W Ketterle, *Opt. Express* **2**, 299 (1998), http://www.opticsexpress.org/abstract.cfm?URI=oe-2-8-299
[48] M Naraschewski and D M Stamper-Kurn, *Phys. Rev. A* **58**, 2423 (1998), DOI: 10.1103/PhysRevA.58.2423